An efficient local moving thermal-fluid framework for accelerating heat and mass transfer simulation during welding and additive manufacturing processes

Yabo Jia, Yassine Saadlaoui, Eric Feulvarch, Jean-Michel Bergheau

An efficient local moving thermal-fluid framework for accelerating heat and mass transfer simulation during welding and additive manufacturing processes

Yabo Jia[a], Yassine Saadlaoui[b], Eric Feulvarch[b], Jean-Michel Bergheau[b]

[a] *INSA Hauts-de-France, CNRS, UMR 8201 – LAMIH, F-59313, Valenciennes, France*
[b] *University of Lyon, Ecole Centrale de Lyon-ENISE, LTDS, UMR 5513 CNRS, 58 rue Jean Parot, Saint-Etienne Cedex 02, 42000, France*

Abstract

Numerical prediction of melt pool morphology and temperature distribution of thermomechanical processes (welding, additive manufacturing) plays an important role in understanding the relationships between process parameters and the quality of manufactured parts. The heat conduction models are limited in their predictability because the transport phenomena relevant to the melt pool dynamic are ignored. In contrast, the multiphysics model allows consideration of the heat transfer, free surface evolution, and transport phenomena in the melt pool, leading to more accurate predictions. However, the computational cost of multiphysics models makes them impractical for part-scale simulations. In this paper, a local moving thermal-fluid framework based on the finite element method is presented, which allows solving the thermal-fluid problem only in the small moving zone containing the melt pool and the heat transfer problem in the rest part. Therefore, this new proposed moving thermal-fluid (MTF) framework is predictive as well as the full thermal-fluid model, while it is much more efficient than a full thermal-fluid model since there are much fewer degrees of freedom (DOF) to solve. Finally, numerical validation tests in welding and additive manufacturing simulations highlight its computational efficiency and high-fidelity, and a relative error of less than 2.6% was observed. In the part-scale simulation of laser welding benchmark, the MTF model takes only 62 hours in place of about three weeks required by a full thermal-fluid model.

Keywords: multiphysics model, finite element method, ALE, moving thermal-fluid framework, welding, additive manufacturing

1. Introduction

Traditionally, optimizing fabrication parameters has relied on experimental trial and error tests, which can be expensive and tricky. Moreover, experimental measurements may not provide the required quantities of interest at all points of the structure. Nowadays, the development of numerical/physical models and computing capabilities has made numerical methods an essential decision-making tool for predicting the consequences of manufacturing processes [1, 2] and optimizing fabrication parameters. Numerical methods provide a cost-effective and efficient way to predict the behaviour of the system, enabling design engineers to assess the impact of design choices on the final product. Therefore, numerical methods have become an indispensable tool in the manufacturing industry.

Thermomechanical processes, such as welding and additive manufacturing, involve a moving heat input that leads to microstructural modifications, distortions, and residual stresses. Numerical simulation of these processes is crucial for understanding the underlying physical phenomena [3, 4, 5]. In thermomechanical processes, the thermal model used to predict the melt pool and thermal history is of importance as it is used to impose variable thermal loading in a subsequent mechanical simulation. Thermal models can be classified as either heat transfer models [6, 7, 8] or multiphysics models [9, 10, 11] depending on the physical phenomena involved. Heat transfer models consider only heat transfer phenomena, while multiphysics models account for other relevant physical phenomena such as free surface and transport phenomena in the melt pool.

The heat transfer model initially consists in solving the heat conduction problem, and numerous physical phenomena are neglected. Various contributions have been made to improve the predictability of the heat transfer model. Goldak *et al.* [12] proposed a volume source of double ellipsoid configuration to consider the transport phenomena in the melt pool. Similarly, different heat source distributions, such as 3D conical Gaussian heat source [13] and cylindrical heat source [14], are developed to model laser or electron-beam welding process. A comparison of the performance of different heat source models in simulating laser butt welding is performed [15], and 3D conical with cylindrical heat source yields better measurements. Apart from the application of volume source, the equivalent thermal conductivity [16, 17] has

also been applied to consider the convective effects, and this method consists in increasing of the heat conduction in the fusion zone. Then, the metallurgical models [18, 19, 20], metal deposition modeling [21, 22, 23], and latent heat due to phase changing between solid and liquid [24, 25] have also been implemented to render the model more physical. Recently, JIA *et al.* [26] presented a steady-state thermal model for rapid predicting melt pool size, which allows taking phase transformation, non-linear properties, and convective effects into consideration. To conclude, the complexity of multiphysics and multi-interactions is reduced to the calibration of the heat source parameters or the enhancement factor of heat conductivity. Thus, the heat transfer model is generally adapted to enrich the existing experimental database, and the quality of the heat transfer model is guaranteed only for the calibrated test cases.

The multiphysics model aims to model the transport phenomena and free surface evolution in the melt pool, and heat transfer in the solid state. The conservation equations (mass, energy balance, momentum) should be solved for each moment and in each element/cell, and the free surface evolution can be tracked by Arbitrary Lagrangian Eulerian method (ALE) [27] in finite element method, volume of fluid (VOF) [28] and Level-Set [29] in Computational Fluid Dynamics (CFD). Compared to ALE free surface tracking method, VOF and Level-Set are much more sophisticated and allow modeling the presence of "keyhole" [30, 31], the formation of porosity [32] and vaporization [33]. The aforementioned methods (VOF, Level-Set) can easily deal with topological changes; however, one major disadvantage of these methods is the numerical diffusion of the diffuse interface, which eventually leads to a loss in precision and a lack of mass conservation [34, 35]. Moreover, these simulations are extremely expensive as both air and metal should be meshed together, and extremely fine mesh is required at the interface for tracking free surface evolution. Recently, Li *et al.* [36] has succeeded in reducing computational costs by implementing a multi-mesh finite volume method for heat transfer and fluid flow problems. They employed a Dirichlet boundary condition to create interaction between the fine and coarse meshes. However, their applications are still limited in modeling domains that are smaller than 5 mm^3 with more than 1 million elements.

In certain normal manufacturing conditions, such as laser welding and direct energy deposition (DED), the presence of "keyhole" should be avoided. In this context, the ALE method is suitable to simulate these processes. In the literature, Kumar *et al.* [37] studied the effect of melt pool convec-

tion, which proved that the Marangoni–Benard convection is dominant in fluid flow dynamics. A 2D transient thermal-fluid model [38] has been proposed to investigate the phenomena responsible for deleterious surface finish. Wirth *et al.* [39] proposed a physical modeling and predictive simulation of the laser cladding process, where all the input parameters are obtained from measurements without compromising assumptions or calibration. Multiphysics models offer attractive features for predicting unknown fabrication parameters. The main challenge is how to reduce the computational cost so that these models can be used in part-scale simulations.

In the current study, a computationally efficient framework based on the finite element method is developed for accelerating the thermal-fluid simulations, and thus make possible multiphysics model applications in part-scale simulations. Surface tension effects ("curvature effect" and the "Marangoni effect"), and buoyancy forces are considered in thermal-fluid computation, and the free surface is explicitly tracked by ALE method. A special tetrahedral element is developed in this context, which allows updating its DOFs automatically according to its state definition at each time step. The proposed framework accelerates considerably the multiphysics simulations by splitting the entire model into a small moving thermal-fluid computational zone and a heat conduction computational zone for the rest, and consequently the ALE procedure is performed uniquely in this small moving thermal-fluid computational zone. Compared to performing thermal-fluid computation in the entire model, these simplifications will greatly reduce the number of DOF of the problem, which leads to a smaller matrix for computing, a smaller RAM space for storing and consequently less CPU time. Finally, this new model is applied to laser welding and DED simulations, and the model is validated through the comparisons of melt pool morphology and temperature evolution with numerical references and experimental measurements .

The paper is organized as follows:

- The numerical models (thermal-fluid, heat transfer) and framework are detailed in Section 2, and it consists of three parts: thermal-fluid problem, heat conduction problem, and moving thermal-fluid framework.

- The validation tests (laser welding, DED) are presented in Section 3, where a laser welding benchmark is employed to validate the numerical/physical models. Applications will highlight the computational efficiency and high-fidelity of proposed model.

- Conclusions and perspectives are given in Section 4.

2. Numerical model

In the numerical modeling of the thermomechanical process (welding, DED), different modes of heat transfer must be taken into account depending on the state of the material:

- Heat conduction including transport phenomena in the liquid state (in the melt pool). The heat equation must then be coupled to fluid dynamics equations.
- Only heat conduction in the solid state.
- Convection in ambient air and radiation losses must be taken into account as boundary conditions of the heat equation on all the external surfaces.

Figure 1 shows the principle of modeling strategy developed in this paper, which consists in creating a moving thermal-fluid computational zone associated with the laser beam. In the thermal-fluid computational zone (TFCZ), which includes the melt pool, the mass/energy/momentum conservation equations will be solved. In the heat conduction computational zone (HCCZ), only the heat conduction equation will be solved. In this paper, one should also note that the TFCZ will be defined by a cubic box for simplicity, and this cuboid should be larger than the size of the melt pool.

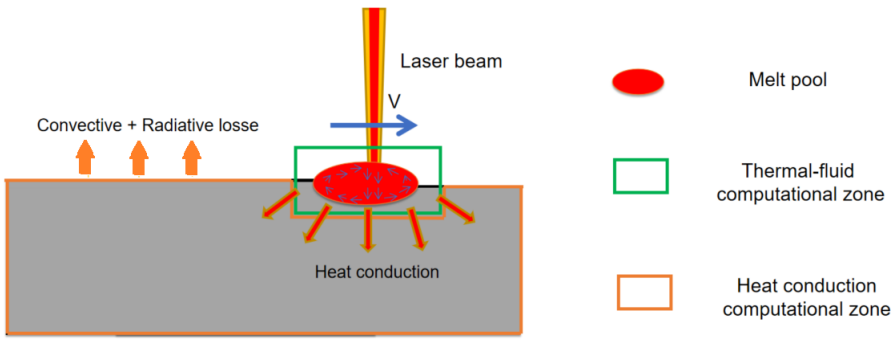

Figure 1: A schematic overview of proposed modeling strategy

To facilitate the transformation of the elements from thermal-fluid computation to heat conduction computation (or vice versa) without remeshing, only tetrahedral mesh are employed (see from Figure 2). The element P1+P1 [40, 41] is employed in TFCZ for the discretization of conservation equations, and P1 element [42] is used in HCCZ.

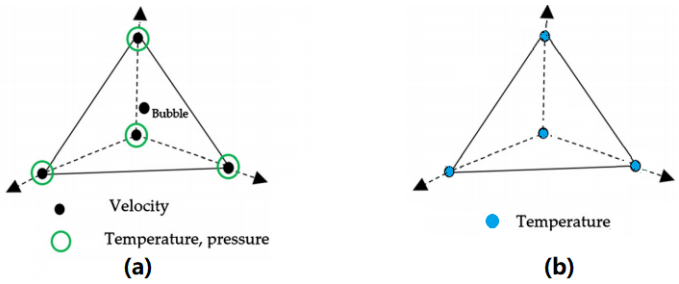

Figure 2: Element type : (a) P1+P1 element; (b) P1 element.

Algorithm 1 details the global resolution procedure that has been developed to accelerate multiphysics simulations. Furthermore, the interface between elements in TFCZ and elements in HCCZ share the same node and nodal temperature, therefore, no special boundary conditions at interface are necessary.

In the rest of this section, we will first introduce governing equations of the thermal-fluid problem and heat conduction problem. The boundary conditions, including surface tension, ALE approach for the actualization of free surface and modeling of heat exchange with air, are exhibited. Finally, the framework for creating a moving thermal-fluid computational zone is detailed in the second place. All the implementations have been realized in $SYSWELD^{TM}$ software [43], but this algorithm can also be achieved using other software, such as Comsol or OpenFOAM.

Algorithm 1 The global resolution procedure

Input: material properties, processing parameters, mesh.
while $t \leq t_{total}$ **do**
    Step 1: Separating different computational zone
    procedure CREATION OF TFCZ AND HCCZ (0, t_{total})
        Calculation the position and size of TFCZ (defined by a cubic **box**).
        loop 3D element
            if Centre of gravity of element is in **box**, **then**
                - Add element into element group TFCZ
            else
                - Add element into element group HCCZ
            end if
        end loop
    end procedure

    Step 2: Resolution of heat and mass transfer problem
    procedure DISCRETIZATION OF GOUVERNING EQUATIONS (0, t_{total})
        if Element is in element group TFCZ, **then**
            - Discretization of mass/energy/momentum conservation equations by P1+P1 element
        else
            - Discretization of heat conduction equation by P1 element
        end if
    end procedure
    - Establishing global matrix
    - Applying thermal initial conditions and boundary conditions
    - Solving global equilibrium equations

    Step 3: ALE procedure in TFCZ
    procedure ELASTIC COMPUTATION (0, t_{total})
        - Free surface tracking
        - Reposition of nodes inside melt pool
    end procedure
    - Updating the geometry of entire model
    - New computing time: $t = t + \Delta t$
end while

2.1. Resolution procedure in the TFCZ

Figure 3 illustrates the resolution procedure of the thermal-fluid problem in the TFCZ, the free surface tracking by the ALE method, and the updating of nodal positions in the melt pool. After the thermal-fluid computation, the elements in the thermal-fluid computational zone can be classified (liquid element, non-liquid element) based on element temperature, and the nodes of liquid elements can be moved.

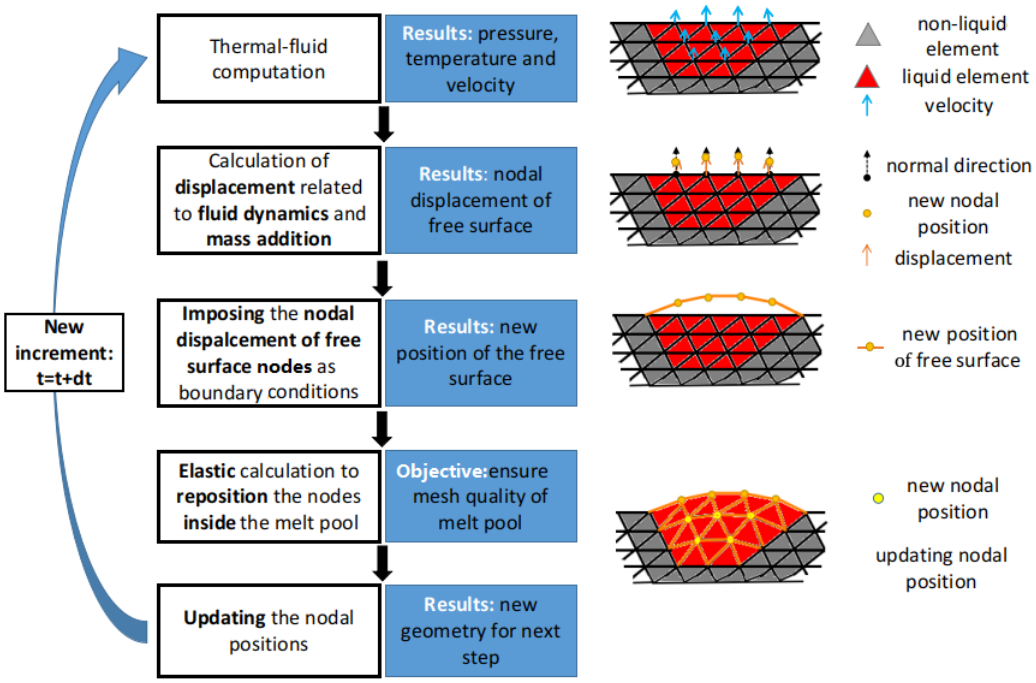

Figure 3: A schematic workflow of thermal-fluid modeling

2.1.1. Governing equations of thermal-fluid problem

For simplifying the numerical model, several assumptions have been made as follows:

- The fluid in the melt pool is assumed to be Newtonian, laminar, thermally dilatable, and mechanically incompressible.
- A Gaussian distribution of the laser beam heat source is assumed.

- In DED simulations, the distribution of powder flow is assumed to be Gaussian, and the powder falling in the melt pool has the same velocity and temperature as the fluid in the melt pool.

From the definition of Eulerian strain rate $\mathbf{d} = \frac{1}{2}\left(\operatorname{grad}\mathbf{v} + (\operatorname{grad}\mathbf{v})^{\intercal}\right)$, the Eulerian mechanical strain rate can be written as (Eq. (1)):

$$\mathbf{d_m} = \mathbf{d} + \frac{\dot{\rho}}{3\rho}\mathbf{I} \tag{1}$$

where the variation of density (ρ) is due to the thermal dilation effects.

Since the fluid in the melt pool is treated as Newtonian, the stress deviator $\mathbf{s}$ is equal to the multiplication of Eulerian mechanical strain rate $\mathbf{d_m}$ and fluid viscosity μ (Eq. (2)):

$$\mathbf{s} = 2\mu\mathbf{d_m} \tag{2}$$

Then, the Cauchy stress tensor is formulated as (Eq. (3)):

$$\sigma = \mathbf{s} - p\mathbf{I} \tag{3}$$

with p being the fluid pressure.

The **mass conservation** equation can be expressed (Eq. (4)):

$$\operatorname{div}\mathbf{v} + \frac{\dot{\rho}}{\rho} = \operatorname{tr}\left(\mathbf{d_m}\right) = 0 \tag{4}$$

with $\frac{\dot{\rho}}{\rho}$ corresponding to volume change due to thermal expansion.

Then, the **momentum conservation** (Navier-Stokes) equation is written as (Eq. (5)):

$$\rho\left(\frac{\partial\mathbf{v}}{\partial t} + \mathbf{grad}\,\mathbf{v}\cdot\mathbf{v}\right) = -\,\mathbf{grad}\,p + \mathbf{div}\,\mathbf{s} + \mathbf{f_v} \tag{5}$$

where $\mathbf{v}$ is the fluid velocity and $\mathbf{f_v}$ represents the volume forces.

The Buoyancy forces can be expressed in volume force $\mathbf{f_v}$ by (Eq. (6)):

$$\mathbf{f_v} = \rho_0\left(1 - \beta\left(T - T_0\right)\right)\mathbf{g} \tag{6}$$

with $\mathbf{g}$ the acceleration of gravity, ρ_0, the density at the reference temperature T_0, and β the volumetric thermal expansion coefficient.

The curvature and Marangoni effects are modeled by imposing a boundary condition of momentum equation at liquid/gas interface, As proposed in

[44], a hydrostatic stress $\boldsymbol{\sigma_{surface}}$ is imposed to surfacic 2D elements whose nodes coincide with those of the 3D mesh located on the free surface, which is written as (Eq. (7)):

$$\boldsymbol{\sigma_{surface}} = \gamma \mathbf{1}_S \tag{7}$$

where γ denotes the expression of surface tension (temperature dependent or not) and $\mathbf{1}_S$ represent the local surfacic 2D unit tensor.

Finally, the **energy conservation** equation is (Eq. (8)):

$$\rho \left(\frac{\partial H}{\partial t} + \mathbf{v} \cdot \mathbf{grad}\, H \right) - \mathrm{div}(\lambda\, \mathbf{grad}\, T) - Q = 0 \tag{8}$$

where H is the specific enthalpy; λ is the thermal conductivity; and Q is the heat source to simulate heating effects. All the material properties can be temperature-dependent. The finite element formulation of the problem is detailed in [10].

The heat losses by convection and radiation on the boundaries (including free surface of melt pool) exchanging with air are modeled (Eq. (9)):

$$\begin{aligned} q_{\text{convective}} &= h_{\text{conv}}\ (T - T_{room}) \\ q_{\text{radiative}} &= \sigma_s \epsilon \left(T^4 - T_{\text{room}}^4 \right) \end{aligned} \tag{9}$$

where h_{conv} , σ_s, and ϵ are the coefficient exchange with air, Stefan-Boltzmann constant, and surface emissivity, respectively. T and T_{room} are in Kelvin.

The 2D Gaussian energy distribution of the laser power is mostly used to simulate the laser heating effect. The form of heat source can be circle or ellipse, which depends on the experimental measurement. In the current study, the heat source equation will be presented in Section 3.

2.1.2. ALE procedure in TFCZ

After resolving the thermal-fluid problem (refer to Fig. (3)), an ALE procedure is employed to update the geometry [10]. This procedure facilitates the tracking of free surface evolution and the repositioning of nodes, specifically within the melt pool. It is important to note that only the nodes inside the melt pool are relocated, applying the ALE procedure exclusively to the TFCZ. Actualization of free surface is achieved by imposing a displacement at the nodes of free surface (Eq. (10)):

$$\boldsymbol{D_i}(t) = \boldsymbol{V}(t) \cdot \Delta t \cdot \vec{\boldsymbol{n}}_{\boldsymbol{i}} = [\boldsymbol{V_i}(t) + \boldsymbol{V_m}(t)] \cdot \Delta t \cdot \vec{\boldsymbol{n}}_{\boldsymbol{i}} \tag{10}$$

Here $\boldsymbol{V_i}(t)$ is the velocity given by Navier-Stocks equation (Eq. 5). Δt represents the time step. $\boldsymbol{V_m}(t)$ denotes the free surface motion due to mass

addition. $\boldsymbol{V}(t)$ is the sum of $\boldsymbol{V_i}(t)$ and $\boldsymbol{V_m}(t)$. This $\boldsymbol{V_m}(t)$ is equal to 0 in the case of laser welding simulation (without mass addition), otherwise, the $\boldsymbol{V_m}$ is generally defined as (Eq. (11))[45]:

$$\boldsymbol{V_m}(t) = \frac{N m_p \eta}{\rho \pi r_p^2} \exp\left(\frac{-N\left(x^2 + (y - V \cdot t)^2\right)}{r_p^2}\right) \boldsymbol{z} \tag{11}$$

where N is the factor of Gaussian distribution, m_p is the masse deposition rate (unit: kg/s), η is the catchment efficiency, ρ represents the density of deposited material, r_p is the radius of mass deposition, and $\boldsymbol{z}$ is the unit vector in the z direction.

Figure 4 resume the ALE procedure, which consists of three steps: (i) calculating the nodal displacements ($\boldsymbol{S}_i$) by multiplying the nodal velocity ($\boldsymbol{V}_i$) by the time step (Δt), and computing the nodal normal direction ($\vec{\boldsymbol{n}}_i$) of the free-surface node by using the mean value of the normals of the skin elements containing it, (ii) performing an elastic calculation by imposing the displacement ($\boldsymbol{D}_i$) in the nodal normal direction as the boundary condition, and (iii) updating the free surface and nodal positions within the melt pool.

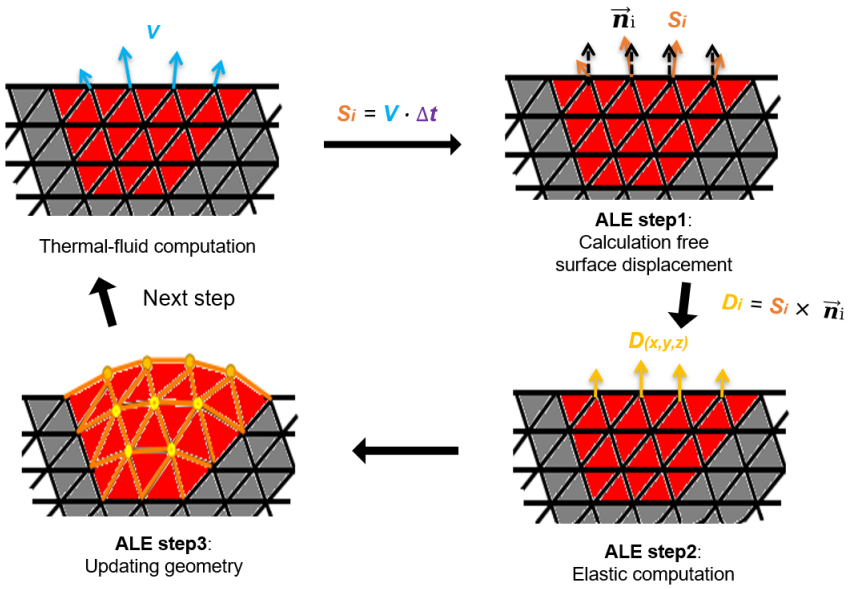

Figure 4: ALE procedure for updating melt pool geometry.

The governing equation of elastic computation is written in classical form, dynamic effects being disregarded:

$$\begin{gathered} \vec{div}\boldsymbol{\sigma} = \vec{0} \\ \text{with } \boldsymbol{\sigma} = \mathbf{C} \cdot \boldsymbol{\varepsilon} \\ \text{and } \boldsymbol{\varepsilon} = \tfrac{1}{2}\left(\mathbf{grad}\,\vec{u} + \mathbf{grad}^T \vec{u}\right) \end{gathered} \tag{12}$$

where $\mathbf{C}$ is the elasticity matrix and $\vec{u}$, the displacement vector. Artificial values for Young's Modulus and Poisson's ratio should be defined to ensure a good mesh quality. Nodes connected to non-liquid elements are prohibited from moving.

In general, the elastic computation is performed for whole model [10], and it is computational efficient as the material behaviour is assumed to be elastic. However, the computational cost of elastic computation becomes non-negligible in part-scale model for two reasons: (i) fine mesh along the heat source trajectory leads to a very large number of DOF; (ii) elastic computation should be performed at each thermal-fluid computational time step.

But only the nodes located at the free surface and inside the melt pool need to be moved. This implies that the elastic computation is exclusively required for the 3D elements within the TFCZ, thus the 3D elements outside the TFCZ can be excluded from the elastic computation, resulting in a significant reduction in matrix size from several hundreds MB to several MB. As a result, the elastic computation becomes much more efficient. Despite the fact that the 3D elements excluded from the elastic computation exhibit zero deformation, it is still necessary to define displacement results at the corresponding nodes. This is crucial for establishing a complete and continuous displacement field throughout the entire model at each time step, as the displacement results are needed latterly for updating the geometry of entire model. Therefore, a subroutine (see Algorithm 2) have been developed to create a full displacement field for all the nodes for the entire model.

Algorithm 2 Creation of a complete displacement field for each time step

Step 1: Input mesh: entire model
Step 2: Calculation of nodal normal direction for nodes at free surface
Step 3: Elastic computation for element group TFCZ:
procedure INPUT DATA FOR ELASTIC COMPUTATION (0, t_{total})
    Properties: Young's Module, Poisson coefficient, Melting temperature ($T_{melting}$)
    Boundary conditions:
    - Symmetry conditions (if involved);
    loop 3D element presented in TFCZ,
        if Tempeature of element is **smaller than** $T_{melting}$, **then**
            - Nodes belonging to this element are fixed;
        else
            - Nodes are free of constraints;
        end if
    end loop
    - Imposing displacement $\mathbf{D_i}$ for nodes at free surface
end procedure
Step 4: Resolution of equilibrium equation
Step 5: Extracting the displacement vector $\vec{u_i}$ computed previously
Step 6: Creating a full displacement field for entire model:
procedure RE-CALCULATE THE DISPLACEMENT RESULTS (0, t_{total})
    loop nodes
        if i belongs to a 3D element in group TFCZ , **then**
            - Its displacement is equal to $\vec{u_i}$;
        else
            - Its displacement is equal to $(0, 0, 0)$;
        end if
    end loop
end procedure
Step 7: Updating the geometry

2.2. Problem to solve in the HCCZ

In the present study, heat transfer analysis is performed using P1 elements. Because the interaction between laser and material is taken into account in the thermal-fluid computational zone, it is no more necessary to introduce a heat source term in the heat equation. Governing equation for

heat conduction problem is given by Eq. 13:

$$\rho\left(\frac{\partial H}{\partial t}\right) - \mathrm{div}(\lambda\,\mathbf{grad}\,T) = 0 \tag{13}$$

Similar to the modeling of heat losses presented in Section 2.1, the Newton's law (Eq. (9)) is employed to model heat convection and radiation between the surface and environment. The finite element formulation of this problem is very classic and can be found, for example, in reference [2].

2.3. Moving thermal-fluid framework

The idea of the moving thermal-fluid framework is to define a rectangular parallelepipedal box that will move together with the heat source (laser) and contain the melt pool at each time. In contrast to the moving reference frame technique outlined in existing literature [46, 47, 48], the framework proposed here offers the advantage of resolving problems associated with arbitrary trajectory shapes and non-constant loading conditions.

This rectangular parallelepipedal box is defined by 4 geometrical parameters (a, b_1, b_2, c) as shown in Fig. 5.

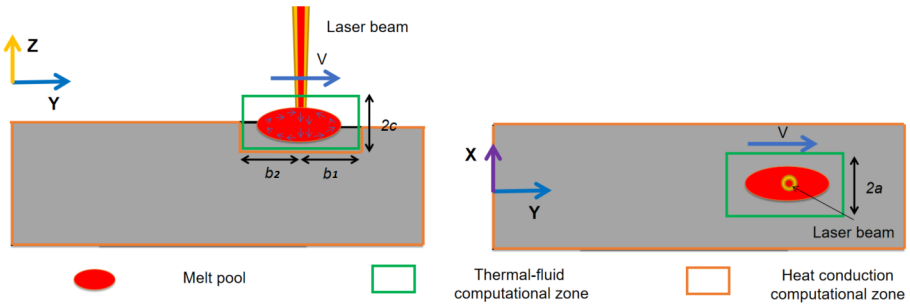

Figure 5: Parameters for defining the box of TFCZ.

As it is known that thermal-fluid computation requires a very fine mesh (an element size of about 10 μm - 500 μm), and it is advised to use the coarse mesh in heat conduction computational zone to minimize the computational cost. In order to simplify the meshing operations and avoid costly remeshing operation, a fine tetrahedral mesh is prepared. Figure 6 shows an incremental schema in 2D for explaining the moving thermal-fluid computational box, and a special subroutine is implemented for the transformation from thermal element to thermal-fluid element (or vice versa).

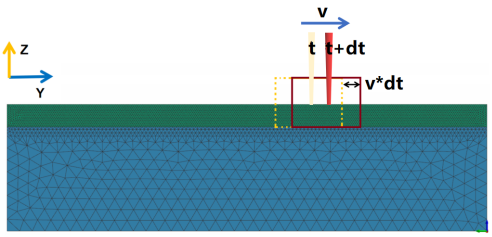

Figure 6: Incremental schema for representing the box displacement

Figure 7 shows the flowchart for separation of heat conduction computation and thermal-fluid computation and the transition between P1 element to P1+P1 element (or vice versa). As is shown in the flowchart, the transformation of the P1 element into the P1+P1 element is accomplished by adding new DOF (pressure field, velocity field), and these new DOF will be initialized at the same time. On the contrary, the inverse transformation is achieved by keeping only the temperature field calculated from the last time step. In general, the removal or addition of DOF has a negligible impact on the numerical results. This is due to the fact that the variations in velocity and pressure within these solid state elements are very small, and thus thermal inertia and volume changes of these elements are insignificant.

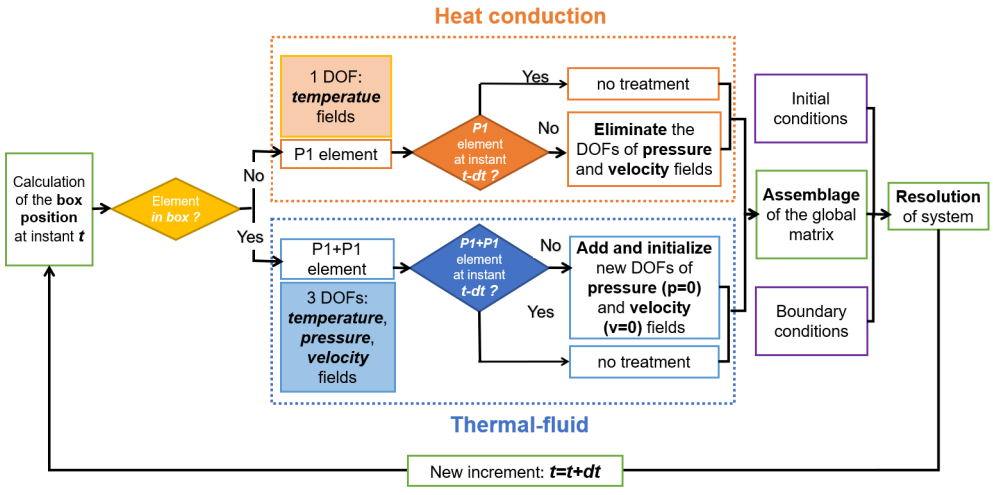

Figure 7: Schema global for separating the thermal-fluid computation and heat conduction computation.

The proposed moving thermal fluid framework offers a significant reduc-

tion in computation time. However, a potential drawback is that the conservation of mass may not be respected for the elements switched from the TFCZ to the HCCZ, because these elements do not have sufficient time to cool down to room temperature and the mass conservation is not solved in HCCZ. Even though the volume change due to thermal expansion is relatively minor, it is always better to incorporate this effect whenever feasible. Since the volume change can not be modeled in HCCZ, the simplest way is thus to apply a constant density when the material temperature is lower than the melting temperature, and volume change is modelled only in melt pool. Furthermore, to prevent instability in velocity solutions at the interface of TFCZ and HCCZ, the nodes positioned on the boundary of the TFCZ are constrained.

3. Validation tests

In this section, we will present two type of applications: (i) laser welding case studies and (ii) DED simulations. For comparing the computational efficiency, all the simulations are performed with the same PC (intel i9-11950H @ 2.60GHz * 6 thread with RAM of 16 Gb).

The proposed numerical model will be applied to laser welding simulation, and the experimental benchmark [8] results are used to validate the numerical models and physical models. The diameters of laser beam and laser power have been measured experimentally (see Fig. 13), and a general Gaussian heat source (Eq.14) is selected to describe the laser energy distribution.

$$\mathrm{Q(x, y, z)} = \frac{B\eta P}{\pi r_x r_y} \cdot exp(-\frac{Bx^2}{r_x^2} - \frac{B(y - V \cdot t)^2}{r_y^2}) \tag{14}$$

where P, η, V and t are the laser power, coefficient of energy absorptivity, laser moving speed and time respectively. B and $r_{x,y}$ denote the parameters of Gaussian distribution of laser beam.

Table 1 presents the thermal-physical properties of AISI 316L employed in this study. The material properties are taken from the literature, and all the properties are temperature-dependent. The melting temperature is of 1500 $^{\circ}C$.

The coefficients of convective loss ($h_{conv} = 20\ W/m^2$) and radiative loss ($\epsilon = 0.8$) at the boundary are taken from the literature [52]. The ambient temperature of air is $T_{air} = 301.15\ K$. For simplicity, the aforementioned

Table 1: Material properties of 316L stainless steel [49, 50, 51].

Parameters	20 °C	1400 °C	1500 °C	2800 °C
Thermal conductivity [W/mK]	14.7	28.0	28.3	28.3
Specific heat [J/(kg·K)]	450	677	677	677
Density [kg/m^3]	8000	8000	7300	7300
Dynamic viscosity [Pa s]	100	100	0.007	0.007
Surface tension [N/m]	-	1.51	-	-
Surface tension gradient [N/(m·K)]	-	$8.65*10^{-4}$	$8.65*10^{-4}$	$8.65*10^{-4}$

properties and thermal boundary conditions are employed for the following validation tests.

In the current study, two types of validation for the MTF model are conducted:

1. **Validation against Numerical Models:** This validation involves comparing the results obtained from the MTF model with outcomes generated by referential numerical models. In this type of validation, the focus is primarily on assessing the quality of the numerical solution. The physical models are held constant and are of relatively lesser importance. This validation is carried out in Section 3.1 and Section 3.2.

2. **Validation against Experiments:** This validation entails comparing the numerical results with experimental data. This validation is to assess the accuracy and quality of both the physical model(s) and the numerical model utilized in the simulation (See section 3.3). For example, the material properties used in the simulations.

These two forms of validation collectively provide a comprehensive assessment of the MTF model's effectiveness and reliability.

3.1. Numerical validations - laser welding

To validate the proposed model, a relatively small numerical model with dimensions of $15.2mm \times 3.16mm \times 2.24mm$ is presented initially. The total simulation time is 100 seconds, consisting of 0.4 seconds of heating and 99.6 seconds of cooling.

Figure 8 provides an overview of the validation tests and the corresponding mesh used in the simulations. The energy distribution of the laser beam

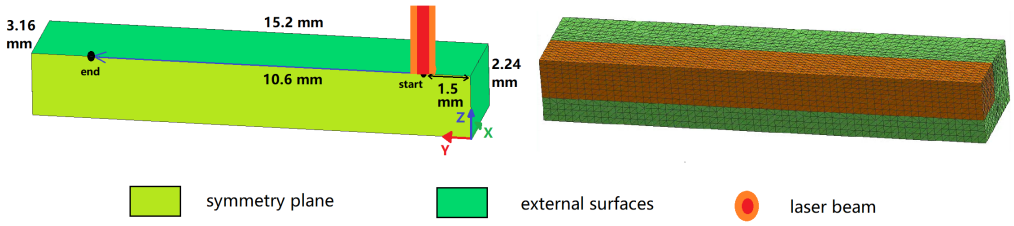

Figure 8: The dimensions and mesh (70272 3D elements and 13702 nodes) of numerical example.

is defined by Eq. 14 and the specific parameters are listed in Table 2. Material properties, such as thermal conductivity and specific heat, are presented in Table 1. Heat losses at the external surfaces are accounted by Eq. 9, while the symmetry plane is considered adiabatic. The displacement of the nodes located at symmetry plane should also respect the symmetry condition, which means that the displacement out of plane is not allowed.

Table 2: Heat source parameters

P	B	η	r_x (mm)	r_y (mm)	v_y (mm/min)
2500 W	2.0	0.3	1.20	0.80	1600

In this numerical case, two numerical models are utilized to demonstrate the efficiency of the proposed model. The first model, referred to the "Classical model", involves conducting thermal-fluid computations for all the 3D elements in orange colour. Therefore, an elastic computation is performed for entire model at each time step. The numerical results of classical model are served as the referential numerical results. The second model, known as the "MTF model" relies on the MTF framework. The box size are defined by the following parameters ($a = 2.0\ mm$, $b_1 = 1.5\ mm$, $b_2 = 2.5\ mm$, $c = 1.386\ mm$), where the box is larger than melting pool size. The same time step ($\Delta t = 5 * 10^{-5} s$) is adopted for two numerical models.

Figure 9 shows the velocity result and melting pool boundary at $t = 0.31295 s$. The comparisons illustrate again that MTF model can reduce the dimensions of thermal-fluid computational zone and consequently the computing time. The velocity field as well as the boundary of melting pool predicted by two models are extremely close, which allows preliminary vali-

dating the proposed model.

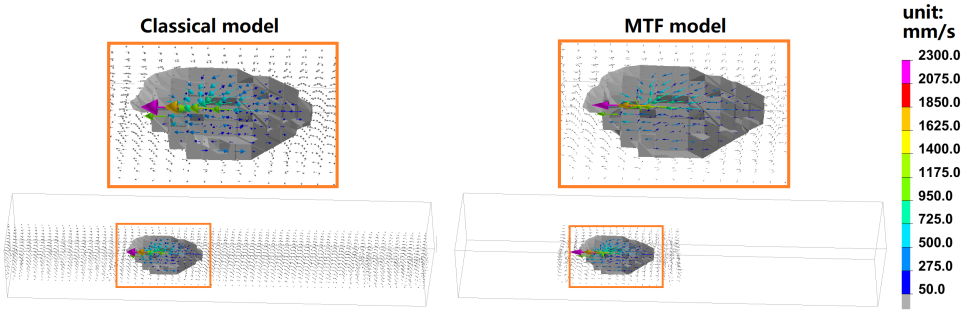

Figure 9: Velocity field and melting pool boundary (surface in grey) simulated by Classical model and MTF model.

Figure 10 shows the temperature distribution and melting pool dimension at $t = 0.31295s$ simulated by Classical model and proposed MTF model. Figure 10-(a) provide the comparison of temperature distribution of entire model, where the MTF model yields well with the numerical reference given by classical model. The comparison of melting pool size (Figure 10-(b)) also confirm the accuracy of proposed MTF model.

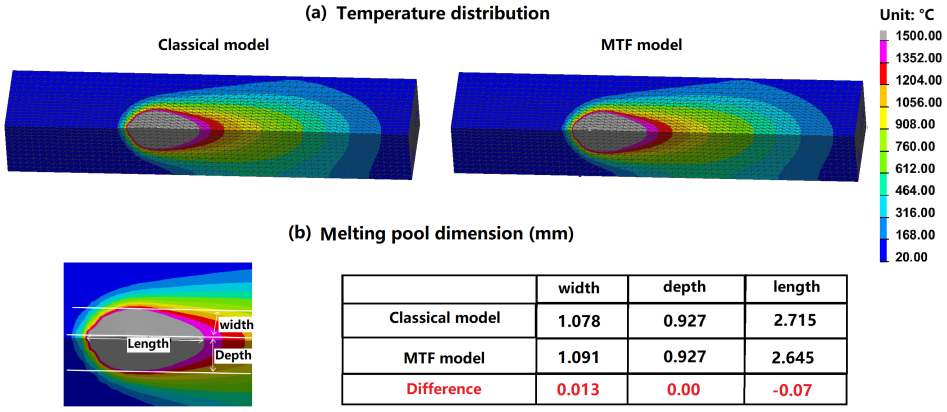

	width	depth	length
Classical model	1.078	0.927	2.715
MTF model	1.091	0.927	2.645
Difference	0.013	0.00	-0.07

Figure 10: Temperature distribution and melting pool dimension simulated by Classical model and MTF model.

Turning now the comparison of computational cost, Table 3 offers a detailed overview of the CPU time, RAM usage, and disk space requirements for each time step. The ratio result is obtained by dividing the computational resources of the MTF model by those of the Classical model. One

should note that the volume ratio of TFCZ between Classical model and MTF model is 37.7%. In this context, RAM-TF denotes the random-access memory needed for storing the matrix necessary for the global thermal-fluid and heat transfer simulation. Similarly, RAM-Elastic signifies the amount of RAM utilized for elastic computations during the ALE procedure. The same nomenclature applies to the CPU utilization as well. One can conclude that the MTF model showcases advantages over the Classical model across all aspects.

Table 3: Computational cost related to Classical model and MTF model.

	CPU-TF (s)	RAM-TF (MB)	CPU-Elastic (s)	RAM-Elastic (MB)	Disk space (MB)
Classical model	3.31	319.0	1.83	183.9	245.8
MTF model	1.93	97.4	0.52	13.4	113.5
Ratio	58.38%	30.40%	28.4%	7.28%	46.17%

Certainly, enlarging the TFCZ is always possible. To investigate the influence of box size, figure 4 provides the simulated melt pool size with different box length ($b_1 + b_2$). By increasing the size of TFCZ, we can achieve results that are closer to the numerical reference. The larger TFCZ is, the better the alignment with the numerical reference becomes, while the more computing time will be required.

Table 4: Simulated melt pool size with different box length.

	width (mm)	depth (mm)	length (mm)
$b_1 = 1.5$, $b_2 = 2.5$	1.091	0.927	2.645
$b_1 = 2.0$, $b_2 = 3.0$	1.085	0.927	2.675
Classical model	1.078	0.927	2.715

3.2. Numerical validations - DED simulations

The main aim of DED case studies is to illustrate the possibility of accelerating the additive manufacturing simulations (such as DED, wire laser additive manufacturing, laser powder additive manufacturing, etc.) by application the idea of MTF framework. Therefore, both Classical model and MTF model are used to simulate DED process.

For the sake of simplicity, we have employed the identical material properties (see Table 1), welding parameters, boundary conditions, and mesh configuration (as shown in Figure 8) from the laser welding case for this DED simulation. Furthermore, we have maintained the same process duration. The parameters of the heat source are outlined in Table 5. Additionally, the dimensions of the box are defined by the following parameters: $a = 2.0$ mm, $b_1 = 1.5$ mm, $b_2 = 3.0$ mm, and $c = 1.386$ mm.

Table 5: Heat source parameters

P	B	η	$r_x(mm)$	$r_y(mm)$	$v_y(mm/min)$
2500 W	2.0	0.2	1.20	0.80	1600

As we have explained in the section 2.1.2, the mass addition in DED process is represented by the velocity calculated from the Eq.11. Some basic assumptions have been made and presented in the beginning of Section 2. The mass addition parameters used in this study are shown in Table 6. The same thermal boundary conditions shown in figure 8 are applied in DED simulations. The powder deposition starts at $t = 0.1$ s and ends at $t = 0.4$.

Table 6: Mass deposition parameters in Eq.11.

Parameters	N	$m_p(kg/s)$	η	$\rho(kg/m^3)$	$r_p(m)$	$v_y(mm/min)$
Value	3	0.001	1	8000	0.002	1600

Figure 11 resume the comparison of temperature field at $t = 0.2677$ s, and three cross-sections are presented for a closer inspection of the difference. The temperature result of MTF model gives perfect correlation with that of Classical model.

Table 7 provides a comparison of the melting pool size at $t = 0.2677$ s, and the dimensions of melting pool are measured in the same way as it is shown in figure 10. The heigh means the difference measured in Z direction

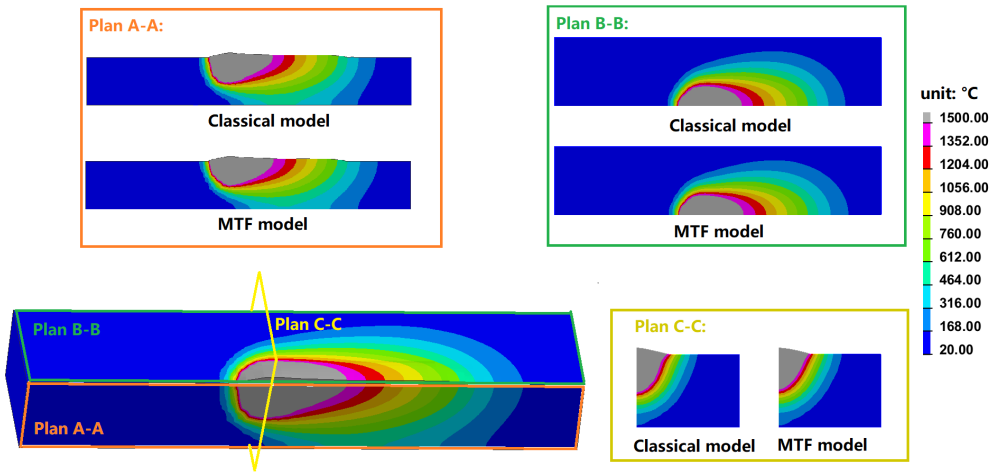

Figure 11: Comparison of temperature distribution predicted by Classical model and proposed MTF model.

between the highest point at the free surface of melting pool and the lowest point at the top surface. It is apparent from this table that a negligible difference has been observed, and we can conclude that MTF model is as predictive as the Classical model.

Table 7: Melting pool size simulated by Classical model and MTF model.

	width (mm)	depth (mm)	length (mm)	height (mm)
Classical model	0.951	1.176	2.988	0.210
MTF model	0.949	1.134	2.998	0.214
Difference	-0.002	-0.038	-0.010	0.004

The comparison of computational cost of each step in the DED simulations is shown in Table 8. The volume ratio of TFCZ between Classical model and MTF model is 42.5%. The MTF model requires less computational resources than Classical model. As a result, the MTF model stands out for its significantly improved computational efficiency, all the while maintaining the accuracy of predictions.

3.3. Numerical and experimental laser welding case study

The validations of the numerical model mentioned above are achieved by comparing the results with those obtained using a numerical reference, where

Table 8: Comparison of computational cost in DED simulation.

	CPU-TF (s)	RAM-TF (MB)	CPU-Elastic (s)	RAM-Elastic (MB)
Classical model	3.52	321.7	1.92	185.3
MTF model	2.12	124.4	0.64	18.8
Ratio	60.23%	38.66%	33.34%	9.82%

the physical model(s) are provided and kept constant. The aforementioned simulations employ a relatively small modeling domains, enabling the simultaneous application of both the Classical model and the MTF model within an acceptable computing time (about 20h for Classical model). The reduction of computing time in aforementioned tests is not significant enough. Now, we would like to apply the proposed model to simulate a real laser welding benchmark and the numerical results are compared and validated against experimental measurements. This comparative analysis allows for the evaluation of the proposed model's accuracy and efficiency.

Figure 12 shows the dimensions of welding sample (100mm x 100mm x 10mm) and locations of thermocouple. The length of weld seam is of $90mm$, and welding velocity is of 2600 mm/min. The material properties of 316L are shown in Table 1. Table 9 presents the calibrated parameters according to experimental measurements [8].

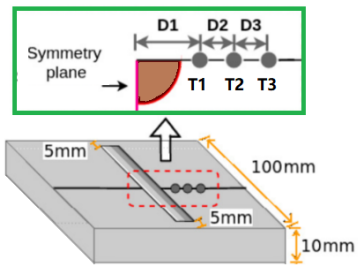

	D1	D2	D3
V2600	2.5±0.2mm	2±0.2mm	2±0.2mm

Figure 12: The dimensions of welding sample and locations of thermocouples.

Thanks to the presence of symmetry plane, only half of the geometry needs to be discretized. Figure 14 presents the mesh for laser welding simulations, and fine elements are meshed in thermal-fluid computational zone, which is slightly larger and deeper than melt pool. The centre of moving box is coincide with the centre of heat source, and the moving box size are defined

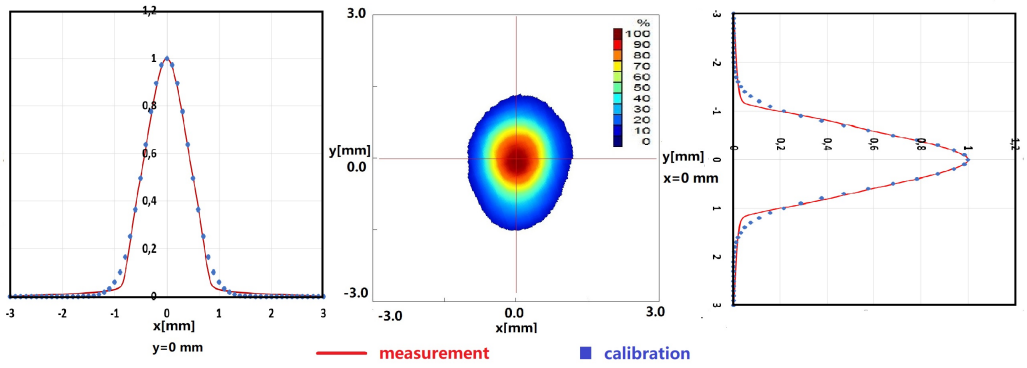

Figure 13: The measured and calibrated energy distribution of laser beam.

Table 9: Heat source parameters used in the simulation of benchmark

P	B	η	r_x (mm)	r_y (mm)	v_y (mm/min)
2500 W	2.5	0.44	1.30	0.90	2600

by the following parameters ($a = 2.0\ mm$, $b_1 = 1.25\ mm$, $b_2 = 3.25\ mm$, $c = 1.386\ mm$). The symmetry plane is supposed to be thermally adiabatic, and the nodes at symmetry plane should respect the symmetry conditions. More details of boundary conditions can be found in the benchmark [8].

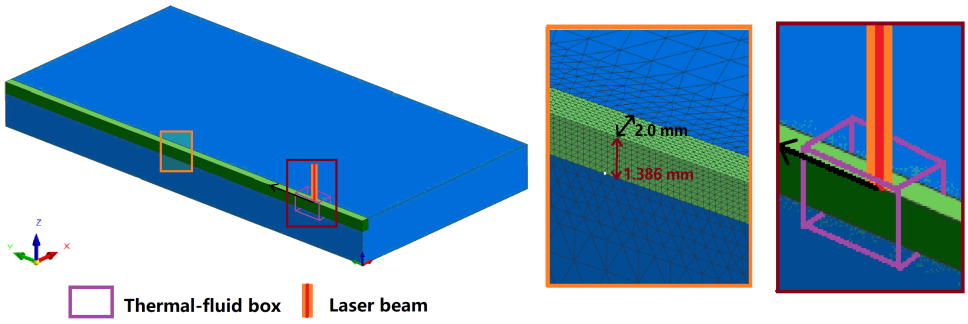

Figure 14: Numerical model and mesh (311,789 3D elements; 56,673 nodes).

Table 10 show a comparison of computational cost of one simulation step, and the acceleration of MTF model becomes more attractive when the modeling domain is much larger. In the current laser welding case study, the Classical model will take about three weeks for completing one simulation.

However, the simulation with MTF model takes about only 61 hours. The MTF model is about 8.3 times faster than Classical model.

Table 10: Comparison of computational cost of each time step.

	CPU-TF (s)	RAM-TF (MB)	CPU-Elastic (s)	RAM-Elastic (MB)
Classical model	28.06	2048	34.81	785.6
MTF model	5.8	132.0	1.8	18.8
Ratio	20.67%	6.45%	5.17%	2.39%

Figure 15 offers a comparison between the weld pool sizes as predicted by the MTF model and experimental measurements. The MTF model effectively predicts the weld pool's length and depth, while an underestimation in weld pool width (approximately 13.1%) is observed. Notably, the negligible height of the weld pool observed in the experimental data is absent in the numerical results. These underestimations could potentially be attributed to the omission of mechanical deformations in the thermal-fluid model or to the incertitude of data of the physical model at high temperature, such as surface tension and the gradient of surface tension.

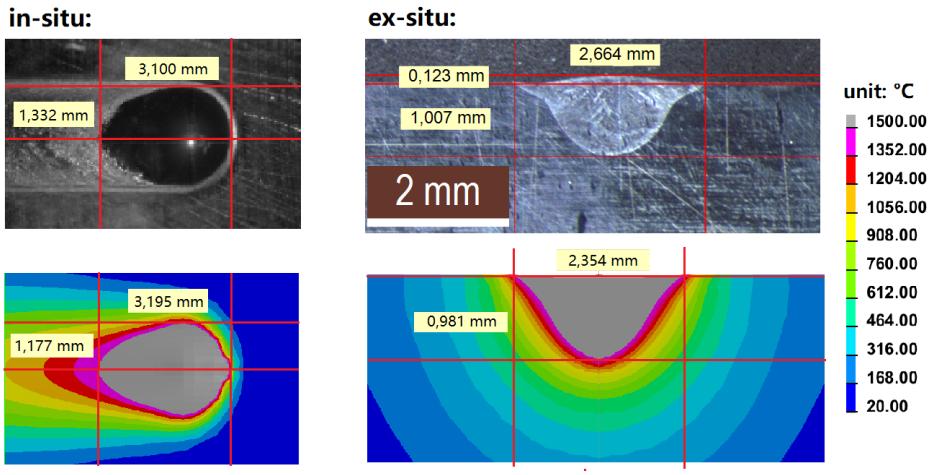

Figure 15: Weld pool size given by experimental measurement and MTF model (unit: mm).

For better inspecting the quality of numerical result, the temperature evolution measured by the thermocouples is also compared to that of MTF

model. In Figure 16, a comparison of temperature evolutions is presented for T1, T2, and T3 (as depicted in Figure 12). Given the inherent uncertainty associated with the positions of the thermocouples, a good correlation with measurements is obtained by using the simulated temperature at positions of $D1 = 2.31$ mm, $D2 = 2.15$ mm and $D3 = 1.81$ mm.

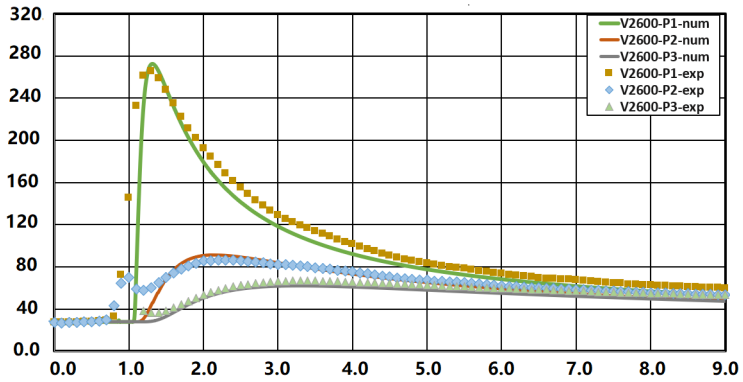

Figure 16: Comparisons of numerical and experimental results of temperature evolution.

4. Conclusion and perspective

This paper presents a local moving thermal-fluid framework for accelerating multi-physics simulations related to thermomechanical processes, such as welding and additive manufacturing. The proposed MTF model consists of splitting the entire model into a moving thermal-fluid computational zone containing the melt pool and a heat transfer computational zone for the rest. A strong coupling between the heat transfer model and the thermal-fluid model is imposed. Compared to the referential numerical results predicted by the Classical model, the numerical validation tests have shown its high fidelity and high efficiency in simulating welding and additive manufacturing processes. Application to a laser welding benchmark shows that the MTF model offers the possibility of simulating a part-scale model within an acceptable computing time.

In the current study, a static refined mesh is applied for the entire melted zone. It is possible to employ the adaptive mesh refinement (AMR) technique to accelerate the simulation, especially for large-scale models. The last application to the laser benchmark highlights the importance of considering mechanical deformation. Therefore, the second perspective concerns

the development of a thermal-hydraulic-mechanical model to account for the mechanical deformation.

5. Acknowledgement

The authors would like to thank Carnot Institute I@L for its financial support as part of the Tortellini project.

References

[1] L.-E. Lindgren, Numerical modelling of welding, Computer Methods in Applied Mechanics and Engineering 195 (48) (2006) 6710–6736, computational Metal Forming. doi:https://doi.org/10.1016/j.cma.2005.08.018.
URL https://www.sciencedirect.com/science/article/pii/S0045782505004834

[2] J.-M. Bergheau, Thermo-mechanical Industrial Processes- Modeling and Numerical Simulation, 2014. doi:10.1002/9781118578759.

[3] M. Dal, R. Fabbro, [invited] an overview of the state of art in laser welding simulation, Optics & Laser Technology 78 (2016) 2–14, the year of light: optical fiber sensors and laser material processing. doi:https://doi.org/10.1016/j.optlastec.2015.09.015.
URL https://www.sciencedirect.com/science/article/pii/S0030399215002595

[4] A. Anca, A. Cardona, J. Risso, V. D. Fachinotti, Finite element modeling of welding processes, Applied Mathematical Modelling 35 (2) (2011) 688–707.

[5] A. J. Pinkerton, Advances in the modeling of laser direct metal deposition, Journal of Laser Applications 27 (S1) (2015) S15001. arXiv:https://doi.org/10.2351/1.4815992, doi:10.2351/1.4815992.
URL https://doi.org/10.2351/1.4815992

[6] J. Reddy, D. Gartling, The Finite Element Method in Heat Transfer and Fluid Dynamics, Applied and Computational Mechanics, CRC Press, 2010.
URL https://books.google.fr/books?id=h7TMBQAAQBAJ

[7] K.-H. Lee, G. J. Yun, A novel heat source model for analysis of melt pool evolution in selective laser melting process, Additive Manufacturing 36 (2020) 101497. doi:https://doi.org/10.1016/j.addma.2020.101497.
URL https://www.sciencedirect.com/science/article/pii/S2214860420308691

[8] Y. Jia, Y. Saadlaoui, H. Hamdi, J. Sijobert, J.-C. Roux, J.-M. Bergheau, An experimental and numerical case study of thermal and mechanical consequences induced by laser welding process, Case Studies in Thermal Engineering 35 (2022) 102078. doi:https://doi.org/10.1016/j.csite.2022.102078.
URL https://www.sciencedirect.com/science/article/pii/S2214157X22003240

[9] Y. Zhang, Q. Chen, G. Guillemot, C.-A. GANDIN, M. Bellet, Numerical modelling of fluid and solid thermomechanics in additive manufacturing by powder-bed fusion: Continuum and level set formulation applied to track- and part-scale simulations, Comptes Rendus Mecanique (09 2018). doi:10.1016/j.crme.2018.08.008.

[10] Y. Saadlaoui, Éric Feulvarch, A. Delache, J.-B. Leblond, J.-M. Bergheau, A new strategy for the numerical modeling of a weld pool, Comptes Rendus Mécanique 346 (11) (2018) 999–1017, computational methods in welding and additive manufacturing Simulation numérique des procédés de soudage et fabrication additive. doi:https://doi.org/10.1016/j.crme.2018.08.007.
URL https://www.sciencedirect.com/science/article/pii/S1631072118301761

[11] S. Lin, Z. Gan, J. Yan, G. J. Wagner, A conservative level set method on unstructured meshes for modeling multiphase thermofluid flow in additive manufacturing processes, Computer Methods in Applied Mechanics and Engineering 372 (2020) 113348. doi:https://doi.org/10.1016/j.cma.2020.113348.
URL https://www.sciencedirect.com/science/article/pii/S0045782520305338

[12] J. Goldak, A. Chakravarti, M. Bibby, A new finite element model for welding heat sources, Metallurgical transactions B 15 (1984) 299–305.

[13] S. Tsirkas, P. Papanikos, T. Kermanidis, Numerical simulation of the laser welding process in butt-joint specimens, Journal of materials processing technology 134 (1) (2003) 59–69.

[14] H. Ramey Jr, Transient heat conduction during radial movement of a cylindrical heat source-applications to the thermal recovery process, Transactions of the AIME 216 (01) (1959) 115–122.

[15] J. Rahman Chukkan, M. Vasudevan, S. Muthukumaran, R. Ravi Kumar, N. Chandrasekhar, Simulation of laser butt welding of aisi 316l stainless steel sheet using various heat sources and experimental validation, Journal of Materials Processing Technology 219 (2015) 48–59. doi:https://doi.org/10.1016/j.jmatprotec.2014.12.008.
URL https://www.sciencedirect.com/science/article/pii/S0924013614004944

[16] S. Safdar, A. J. Pinkerton, L. Li, M. A. Sheikh, P. J. Withers, An anisotropic enhanced thermal conductivity approach for modelling laser melt pools for ni-base super alloys, Applied Mathematical Modelling 37 (3) (2013) 1187–1195. doi:https://doi.org/10.1016/j.apm.2012.03.028.
URL https://www.sciencedirect.com/science/article/pii/S0307904X12001916

[17] A. M. Kamara, W. Wang, S. Marimuthu, L. Li, Modelling of the melt pool geometry in the laser deposition of nickel alloys using the anisotropic enhanced thermal conductivity approach, Proceedings of the Institution of Mechanical Engineers, Part B: Journal of Engineering Manufacture 225 (1) (2011) 87–99. arXiv:https://doi.org/10.1177/09544054JEM2129, doi:10.1177/09544054JEM2129.
URL https://doi.org/10.1177/09544054JEM2129

[18] J. Leblond, J. Devaux, A new kinetic model for anisothermal metallurgical transformations in steels including effect of austenite grain size, Acta Metallurgica 32 (1) (1984) 137–146. doi:https://doi.org/10.1016/0001-6160(84)90211-6.
URL https://www.sciencedirect.com/science/article/pii/0001616084902116

[19] K. DP, M. RE, A general equation prescribing the extent of the austenite-martensite transformation in pure iron-carbon alloys and plain carbon steels, Acta Metallurgica 7 (1) (1959) 59–60.

[20] P. Ferro, H. Porzner, A. Tiziani, F. Bonollo, The influence of phase transformations on residual stresses induced by the welding process—3d and 2d numerical models, Modelling and Simulation in Materials Science and Engineering 14 (2) (2006) 117.

[21] L.-E. Lindgren, H. Runnemalm, M. O. Näsström, Simulation of multipass welding of a thick plate, International journal for numerical methods in engineering 44 (9) (1999) 1301–1316.

[22] P. Michaleris, Modeling metal deposition in heat transfer analyses of additive manufacturing processes, Finite Elements in Analysis and Design 86 (2014) 51–60. doi:https://doi.org/10.1016/j.finel.2014.04.003.
URL https://www.sciencedirect.com/science/article/pii/S0168874X14000584

[23] Y. Zhang, G. Guillemot, M. Bernacki, M. Bellet, Macroscopic thermal finite element modeling of additive metal manufacturing by selective laser melting process, Computer Methods in Applied Mechanics and Engineering 331 (2018) 514–535. doi:https://doi.org/10.1016/j.cma.2017.12.003.
URL https://www.sciencedirect.com/science/article/pii/S0045782517307545

[24] C. Bonacina, G. Comini, A. Fasano, M. Primicerio, Numerical solution of phase-change problems, International Journal of Heat and Mass Transfer 16 (10) (1973) 1825–1832. doi:https://doi.org/10.1016/0017-9310(73)90202-0.
URL https://www.sciencedirect.com/science/article/pii/0017931073902020

[25] Y. Jia, Y. Saadlaoui, J.-M. Bergheau, A temperature-dependent heat source for simulating deep penetration in selective laser melting process, Applied Sciences 11 (23) (2021). doi:10.3390/app112311406.
URL https://www.mdpi.com/2076-3417/11/23/11406

[26] Y. Jia, Y. Saadlaoui, J.-C. Roux, J.-M. Bergheau, Steady-state thermal model based on new dedicated boundary conditions – application in the simulation of laser powder bed fusion process, Applied Mathematical Modelling 112 (2022) 749–766. doi:https://doi.org/10.1016/j.apm.2022.08.013.
URL https://www.sciencedirect.com/science/article/pii/S0307904X22003961

[27] C. Hirt, A. Amsden, J. Cook, An arbitrary lagrangian-eulerian computing method for all flow speeds, Journal of Computational Physics 14 (3) (1974) 227–253. doi:https://doi.org/10.1016/0021-9991(74)90051-5.
URL https://www.sciencedirect.com/science/article/pii/0021999174900515

[28] C. Hirt, B. Nichols, Volume of fluid (vof) method for the dynamics of free boundaries, Journal of Computational Physics 39 (1) (1981) 201–225. doi:https://doi.org/10.1016/0021-9991(81)90145-5.
URL https://www.sciencedirect.com/science/article/pii/0021999181901455

[29] S. Osher, J. A. Sethian, Fronts propagating with curvature-dependent speed: Algorithms based on hamilton-jacobi formulations, Journal of Computational Physics 79 (1) (1988) 12–49. doi:https://doi.org/10.1016/0021-9991(88)90002-2.
URL https://www.sciencedirect.com/science/article/pii/0021999188900022

[30] F. Lu, X. Li, Z. Li, X. Tang, H. Cui, Formation and influence mechanism of keyhole-induced porosity in deep-penetration laser welding based on 3d transient modeling, International Journal of Heat and Mass Transfer 90 (2015) 1143–1152. doi:https://doi.org/10.1016/j.ijheatmasstransfer.2015.07.041.
URL https://www.sciencedirect.com/science/article/pii/S0017931015007504

[31] Y. Mayi, M. Dal, P. Peyre, M. Bellet, R. Fabbro, Physical mechanisms of conduction-to-keyhole transition in laser welding and additive manufacturing processes, Optics & Laser Technology 158 (2023) 108811. doi:10.1016/j.optlastec.2022.108811.

[32] W. Chen, W. Wang, A quantitative model of keyhole instability induced porosity in laser welding of titanium alloy, Metallurgical and Materials Transactions A 45 (06 2014). doi:10.1007/s11661-014-2231-3.

[33] A. Queva, G. Guillemot, C. Moriconi, C. Metton, M. Bellet, Numerical study of the impact of vaporisation on melt pool dynamics in laser powder bed fusion - application to in718 and ti-6al-4v, additive manufacturing 35 (2020) 101249, Additive Manufacturing (2020) 101249doi:10.1016/j.addma.2020.101249.

[34] F. de Sousa, N. Mangiavacchi, L. Nonato, A. Castelo, M. Tomé, V. Ferreira, J. Cuminato, S. McKee, A front-tracking/front-capturing method for the simulation of 3d multi-fluid flows with free surfaces, Journal of Computational Physics 198 (2) (2004) 469–499. doi:https://doi.org/10.1016/j.jcp.2004.01.032.
URL https://www.sciencedirect.com/science/article/pii/S0021999104000488

[35] H. Hua, J. Shin, J. Kim, Level Set, Phase-Field, and Immersed Boundary Methods for Two-Phase Fluid Flows, Journal of Fluids Engineering 136 (2), 021301 (11 2013). arXiv:https://asmedigitalcollection.asme.org/fluidsengineering/article-pdf/136/2/021301/6190065/fe_136_02_021301.pdf, doi:10.1115/1.4025658.
URL https://doi.org/10.1115/1.4025658

[36] M.-J. Li, J. Chen, Y. Lian, F. Xiong, D. Fang, An efficient and high-fidelity local multi-mesh finite volume method for heat transfer and fluid flow problems in metal additive manufacturing, Computer Methods in Applied Mechanics and Engineering 404 (2023) 115828. doi:https://doi.org/10.1016/j.cma.2022.115828.
URL https://www.sciencedirect.com/science/article/pii/S0045782522007848

[37] A. Kumar, S. Roy, Effect of three-dimensional melt pool convection on process characteristics during laser cladding, Computational Materials Science 46 (2) (2009) 495–506. doi:https://doi.org/10.1016/j.commatsci.2009.04.002.
URL https://www.sciencedirect.com/science/article/pii/S0927025609001608

[38] S. Morville, M. CARIN, P. Peyre, M. Gharbi, D. CARRON, P. LE MASSON, R. Fabbro, 2d longitudinal modeling of heat transfer and fluid flow during multilayered direct laser metal deposition process, Journal of Laser Applications 24 (3) (2012) 1–9, version post-print de l'article : JLA Vol : 24 Iss:3. 2D longitudinal modeling of heat transfer and fluid flow during multilayered direct laser metal deposition process.
URL https://hal.archives-ouvertes.fr/hal-00799208

[39] F. Wirth, K. Wegener, A physical modeling and predictive simulation of the laser cladding process, Additive Manufacturing 22 (2018) 307–319. doi:https://doi.org/10.1016/j.addma.2018.05.017.
URL https://www.sciencedirect.com/science/article/pii/S2214860418301349

[40] K.-J. Bathe, Finite element procedures, Prentice-Hall.

[41] D. N. Arnold, F. Brezzi, M. Fortin, A stable finite element for the Stokes equations, Ist., Consiglio, 1983.

[42] Finite Element Simulation of Heat Transfer, John Wiley & Sons, Ltd, 2008. arXiv:https://onlinelibrary.wiley.com/doi/pdf/10.1002/9780470611418.fmatter, doi:https://doi.org/10.1002/9780470611418.fmatter.
URL https://onlinelibrary.wiley.com/doi/abs/10.1002/9780470611418.fmatter

[43] SYSWELD^{TM}, *Reference Analysis Manual*, released: 2022, ESI Group.

[44] J.-B. Leblond, H. A. El Sayed, J.-M. Bergheau, On the incorporation of surface tension in finite-element calculations, Comptes Rendus Mécanique 341 (11) (2013) 770–775. doi:https://doi.org/10.1016/j.crme.2013.10.004.
URL https://www.sciencedirect.com/science/article/pii/S1631072113001253

[45] Z. Gan, G. Yu, X. He, S. Li, Surface-active element transport and its effect on liquid metal flow in laser-assisted additive manufacturing, International Communications in Heat and Mass Transfer 86 (2017) 206–214. doi:https://doi.org/10.1016/j.icheatmasstransfer.2017.06.007.

URL https://www.sciencedirect.com/science/article/pii/S0735193317301409

[46] J.-M. Bergheau, V. ROBIN, B. Frédéric, Finite element simulation of processes involving moving heat sources. application to welding and surface treatment, Journal of Shanghai Jiaotong University (Science) E-5 (2000) 114–122.

[47] A. Hacquin, P. Montmitonnet, J.-P. Guillerault, A steady state thermo-elastoviscoplastic finite element model of rolling with coupled thermo-elastic roll deformation, Journal of Materials Processing Technology 60 (1) (1996) 109–116, proceedings of the 6th International Conference on Metal Forming. doi:https://doi.org/10.1016/0924-0136(96)02315-1.
URL https://www.sciencedirect.com/science/article/pii/0924013696023151

[48] Y. Jia, Numerical simulation of steady states associated with thermo-mechanical processes, Theses, Université de Lyon (Dec. 2020).
URL https://theses.hal.science/tel-03736799

[49] G. Knapp, T. Mukherjee, J. Zuback, H. Wei, T. Palmer, A. De, T. DebRoy, Building blocks for a digital twin of additive manufacturing, Acta Materialia 135 (2017) 390–399. doi:https://doi.org/10.1016/j.actamat.2017.06.039.
URL https://www.sciencedirect.com/science/article/pii/S1359645417305141

[50] T. Heeling, M. Cloots, K. Wegener, Melt pool simulation for the evaluation of process parameters in selective laser melting, Additive Manufacturing 14 (2017) 116–125. doi:https://doi.org/10.1016/j.addma.2017.02.003.
URL https://www.sciencedirect.com/science/article/pii/S221486041630313X

[51] H. Fukuyama, H. Higashi, H. Yamano, Thermophysical properties of molten stainless steel containing 5 mass % b4c, Nuclear Technology 205 (9) (2019) 1154–1163. arXiv:https://doi.org/10.1080/00295450.2019.1578572, doi:10.1080/00295450.2019.1578572.
URL https://doi.org/10.1080/00295450.2019.1578572

[52] Y. Jia, J.-M. Bergheau, J.-B. Leblond, J.-C. Roux, R. Bouchaoui, S. Gallée, A. Brosse, A new nodal-integration-based finite element method for the numerical simulation of welding processes, Metals 10 (10) (2020) 1386.